ROYAL SOCIETY OF CHEMISTRY

PAPER

Check for updates

Cellular internalization of polypeptide-based nanoparticles: effects of size, shape and surface morphology†

Jiaxiao Xue,[a] Zhou Guan,[a] Xingyu Zhu,[a] Jiaping Lin, [ID] *[a] Chunhua Cai, [ID] *[a] Xiao Jin,[a] Yongsheng Li, [ID] [a] Zhaoyang Ye,[a] Wenjie Zhang[b] and Xinquan Jiang*[b]

Nanoparticles (NPs) can be taken up by cells; however, the effects of the structural characteristics of NPs on their cellular internalization have not been well explored. In this work, cellular internalization performances of various NPs including rods with helical surface (helical rods), spheres with stripe-pattern surface (striped spheres), and spheres with smooth surface (smooth spheres) were investigated by a combination of experiments and theoretical simulations. This study focuses on the effects of the size, shape, and surface morphology on their cellular internalization behaviors. These NPs were self-assembled from mixtures of fluorescein isothiocyanate (FITC)-labelled poly(γ-benzyl-ʟ-glutamate)-*block*-poly(ethylene glycol) (PBLG(FITC)-*b*-PEG) block copolymers and PBLG or polystyrene (PS) homopolymers. It was found that the NPs possessing smaller size, rod-like shape, and helical/striped surface morphology exhibit higher cellular internalization efficiency. Such differences in the internalization efficiency for the NPs can be attributed to the differences in both their surface areas and internalization pathways. This study could not only guide the design of nanocarriers with enhanced cellular internalization efficiency, but also deepen our understanding of the internalization behavior of natural NPs with similar structures (*e.g.*, virus).

Introduction

Self-assembly of polymers is a promising way to prepare various kinds of nanoparticles (NPs), including spheres, vesicles, disks, helices, and so on.[1–5] The NPs self-assembled from biopolymers (*e.g.*, peptide- and polypeptide-based polymers) possess advantages in biorelated applications, for example, nanocarriers for drug delivery,[6–10] gene technology,[11–14] and photodynamic therapy.[15–19] As nanocarriers for drugs and genes, in most situations, they should pass through cell membranes to reach intracellular targets and display their functions. Many studies have been carried out to explore the internalization process of NPs. Both chemical compositions and physical structures of NPs have been found to affect their cellular internalization behaviors.[6,12,13] Currently, the influence of the chemical characteristics has been well addressed. For example, targeted groups can accelerate the uptake process, and stimuli groups can enhance the release performance of the nanocarriers. These strategies have been widely applied in designing efficient drug delivery systems.[20,21]

Compared with the chemical properties, the effect of the physical structures of NPs has attracted much less attention. Some reports have shown that the structural characteristics of NPs, such as size,[22–25] shape,[26–30] and surface morphology,[31–34] significantly influence their cellular internalization. For instance, Liu *et al.* found that the staggered lamellae have higher uptake efficiency compared to other nanostructures, including spheres, smooth disks, and compound vesicles, due to the rough surface and the clathrin- and caveolae-independent endocytosis process of the staggered lamellae.[26] Meng *et al.* demonstrated that rod-like NPs show higher internalization efficiency than their spherical counterparts.[27] However, most research studies are focused on the effect of one single characteristic of the NPs. There is a lack of compre-

[a]*Shanghai Key Laboratory of Advanced Polymeric Materials, State Key Laboratory of Bioreactor Engineering, Key Laboratory for Ultrafine Materials of Ministry of Education, School of Materials Science and Engineering, East China University of Science and Technology, Shanghai 200237, China. E-mail: jlin@ecust.edu.cn, caichunhua@ecust.edu.cn*
[b]*Department of Prosthodontics, Ninth People's Hospital, Shanghai Jiao Tong University School of Medicine, 639 Zhizaoju Road, Shanghai 200011, China. E-mail: xinquanj@aliyun.com*
†Electronic supplementary information (ESI) available: Reagents and materials, synthesis of polymers, polymer characterization, characterization methods of the NPs, preparation of self-assembled NPs, DLS measurements of the NPs, observation of cells incubated with NPs, coarse-grained simulation model, simulation method, parameter setting, simulation system, cellular internalization of NPs with large sizes. See DOI: 10.1039/c8bm01163j

hensive study concerning the influence of these various structural characteristics of NPs on cellular internalization. Understanding these effects could provide ideas for designing more efficient nanocarriers.

Experimentally understanding the cellular internalization behaviors of NPs usually suffers from difficulties in finding some specific information arising from limited experimental techniques. Theoretical simulation has been applied as an effective tool and provides a deep insight into the internalization process of various NPs.[35–40] For example, Shi *et al.* demonstrated that coarse-grained molecular dynamics (CGMD) simulations not only reproduced the experimental phenomenon that carbon nanotubes enter cells through a tip-first way, but also showed that their entry angles play an important role in the internalization process.[37] In the study of cellular internalization of NPs, by a combination of experimental observations and theoretical simulations, the fundamental mechanisms can be comprehensively revealed.

In this work, we prepared various NPs, including rods with helical surface (helical rods), spheres with stripe-pattern surface (striped spheres), and spheres with smooth surface (smooth spheres), through the cooperative self-assembly of fluorescein isothiocyanate (FITC)-labelled poly(γ-benzyl-L-glutamate)-*block*-poly(ethylene glycol) (PBLG(FITC)-*b*-PEG) block copolymers with PBLG or polystyrene (PS) homopolymers. The effect of the structural characteristics of these NPs, including size, shape, and surface morphology, on the cellular internalization behavior was explored. It was found that the NPs possessing smaller size, rod-like shape, and helical/striped surface morphology exhibit higher internalization efficiency. Moreover, CGMD simulations were conducted to provide a deep insight into the cellular internalization behavior of these NPs. Unique internalization pathways for the helical rods and the striped spheres were revealed. Due to the different structural characteristics of the NPs, they possess different surface areas and internalization pathways, which results in the different internalization efficiencies. We expect that these investigations could help provide a deep understanding of the influence of various structural characteristics of self-assembled NPs on cellular internalization, and inspire the preparation of novel efficient NPs applied in the biomedical field.

Materials and methods

Materials

PBLG(FITC)$_{38\,700}$-*b*-PEG$_{5000}$ block copolymers, PBLG homopolymers (PBLG$_{28\,000}$, PBLG$_{118\,000}$, and PBLG$_{300\,000}$), and PS homopolymers (PS$_{10\,000}$ and PS$_{19\,400}$) were used in this work (the subscripts denote the number average molecular weight of the polymers). Deionized water was obtained from a Millipore Super-Q Plus Water System to a level of 18.2 MΩ cm resistivity. Dialysis bag (MEMBRA-CEL, 3500 molecular weight cutoff) was obtained from Serva Electrophoresis GmbH. The details of the synthesis and characterization of polymers and reagents are provided in the ESI (sections 1.1–1.3†).

Preparation of self-assembled NPs

For the preparation of self-assembled NPs, the PBLG(FITC)-*b*-PEG block copolymers and the PBLG and PS homopolymers were separately dissolved in tetrahydrofuran (THF), *N,N′*-dimethylformamide (DMF), or their mixtures. The polymer concentration of the stock solutions was 0.6 g L^{-1}. Then, 8 mL of the block copolymer solutions and 2 mL of the homopolymer solutions were mixed together. 2.5 mL deionized water was added to the mixed solutions at a rate of 0.02 mL s^{-1} with vigorous stirring. Finally, the solution was dialyzed against deionized water to remove the organic solvents. All the preparation procedures were conducted at 20 °C and shielded from light. Short and long helical rods were prepared using the mixtures of PBLG(FITC)-*b*-PEG/PBLG$_{118\,000}$ (initial solvent: THF/DMF, 3/7, v/v) and PBLG(FITC)-*b*-PEG/PBLG$_{300\,000}$ (initial solvent: THF/DMF, 3/7, v/v), respectively. The small and large striped spheres were prepared using PBLG(FITC)-*b*-PEG/PS$_{10\,000}$ mixtures (initial solvent: THF/DMF, 7/3, v/v) and PBLG(FITC)-*b*-PEG/PS$_{19\,400}$ mixtures (initial solvent: THF/DMF, 3/7, v/v), respectively. The small and large smooth spheres were prepared using PBLG(FITC)-*b*-PEG/PBLG$_{28\,000}$ mixtures (initial solvent: THF) and PBLG(FITC)-*b*-PEG/PS$_{19\,400}$ mixtures (initial solvent : DMF), respectively. The details of the preparation procedures of the nanoparticles are provided in the ESI, section 1.4.†

Cellular internalization of FITC labelled NPs

The cellular internalization of these NPs was examined with NIH3T3 cells. The cells were seeded in 24-well plates at 5×10^4 cells per well in 1 mL of Dulbecco's modified Eagle's medium (DMEM), which contained the added constituents of 10% fetal bovine serum (FBS), 100 μg mL^{-1} penicillin, and 100 μg mL^{-1} streptomycin. The cells were cultured at 37 °C for 24 h under a humidified atmosphere of 5% CO$_2$. Then the culture medium was replaced with DMEM containing the NPs (0.09 mg mL^{-1}). The incubation was conducted with a time course from 1 to 8 h. After the incubation, the solution was removed, followed by rinsing of the cells three times with PBS and fixing in 4% formaldehyde for 15 min at 4 °C. The cell nuclei were stained with a DAPI solution for 5 min before analysis by CLSM.

Simulation method

Coarse-grained molecular dynamics (CGMD) simulations were performed in the present work. All of the NPs were constructed using a hydrophobic template decorated with ligands. The template corresponds to the hydrophobic PS and PBLG templates of the NPs, while the ligands denote the hydrophilic PEG corona. For the details of the models of NPs, see the ESI, section 2.1.† The phospholipids which form the bilayer membrane are coarse-grained to three beads connected by harmonic bonds. The head bead of the lipid is hydrophilic, and the two tail beads are hydrophobic. A specific amount of lipids in the membrane are receptors, whose head beads are bound to the ligands on the NPs. Based on this model, a solvent-free simulation method was applied in the simulations.[41] A

Langevin thermostat and a Berendsen barostat were used to achieve a constant temperature and membrane tension in the system.[42–45] For the details of this method, see the ESI, section 2.2.†

Parameters in simulation

The simulations were performed in a box with a size of $70 \times 70 \times 200\sigma$ and $N\Sigma T$ ensemble (σ is the length unit; N, Σ, and T denote the bead number, membrane tension, and system temperature, respectively). The membrane was constructed with 4400 lipids, 50% of which were receptors. Both the rod-like and spherical NPs were modelled by 1010 hydrophobic beads (template) and 131 hydrophilic beads (ligands). The diameter (d) and length (l) of the rod-like NPs were set to 8σ and 32σ, while the radius (r) of the spherical NPs was set to 8σ. In the beginning, the NPs were set above the membrane. After applying an initial velocity to the NPs, the simulations were then conducted for $5 \times 10^5\tau$ (τ represents the time unit). In the study of the uptake percentage of these NPs as a function of time, the initial distance between the NPs and membrane was varied from 0 to 20σ, which can mimic the situation where cells were treated with NPs in solutions. The details of the parameter setting can be found in the ESI, sections 2.3 and 2.4.†

Results and discussion

Characteristics of the self-assembled NPs

The mixtures of $PBLG(FITC)_{38\,700}\text{-}b\text{-}PEG_{5000}/PBLG_{118\,000}$ and $PBLG(FITC)_{38\,700}\text{-}b\text{-}PEG_{5000}/PBLG_{300\,000}$ are able to form helical rods, and the mixtures of $PBLG(FITC)_{38\,700}\text{-}b\text{-}PEG_{5000}/PS_{10\,000}$, $PBLG(FITC)_{38\,700}\text{-}b\text{-}PEG_{5000}/PS_{19\,400}$, and $PBLG(FITC)_{38\,700}\text{-}b\text{-}PEG_{5000}/PBLG_{28\,000}$ self-assemble into spherical structures with a striped or smooth surface (striped spheres or smooth spheres). For the helical rods, the PBLG homopolymers form a rigid bundle, and the PBLG(FITC)-b-PEG block copolymers wrap around the bundle to form a helical shell.[46–48] Similarly, in the spherical structures, the PS or PBLG homopolymers form a sphere, and the block copolymers self-assemble onto the surfaces of the spheres. Depending on the experimental conditions, the block copolymers form a stripe-pattern surface or smooth surface.[49,50]

To conduct a comprehensive study of the influence of the structural characteristics of NPs on their cellular internalization, we chose the NPs by considering the size (hydrodynamic radius (R_h)), the shape (rods $vs.$ spheres), and the surface morphology (striped $vs.$ smooth). It should be noted that for $in\ vitro$ incubation of different shapes of NPs, the R_h of a NP is an important parameter expressing its movement ability in solution, and usually used to represent the size of the NP.[51–53]

Six types of NPs were selected including short helical rods (helical rod-1, $R_h = 111.2$ nm), long helical rods (helical rod-2, $R_h = 164.0$ nm), small striped spheres (striped sphere-1, $R_h = 112.9$ nm), large striped spheres (striped sphere-2, $R_h = 163.3$ nm), small smooth spheres (smooth sphere-1, $R_h = $

114.4 nm), and large smooth spheres (smooth sphere-2, $R_h = 168.5$ nm), respectively. The morphologies of the NPs determined using a scanning electron microscope (SEM) are given in Fig. 1a, b, d, e, g, and h, respectively. The detailed structural parameters of these NPs are given in Table 1. According to the R_h values, these NPs can be sorted into two groups, $i.e.$, smaller NPs with $R_h \approx 113$ nm (group 1) and larger NPs with $R_h \approx 165$ nm (group 2). Since these NPs were fluorescently labelled with FITC, they exhibit green fluorescence. Shown in Fig. 1c, f and i are the typical fluorescent images of helical rod-2, striped sphere-2, and smooth sphere-2, respectively. The details regarding the characterization methods and dynamic light scattering (DLS) measurement of the self-assembled NPs are presented in the ESI, sections 1.5 and 1.6,† respectively.

During the internalization process of the NPs, the surface charges of the NPs have an influence on the interaction between the NPs and cells.[30] Herein, the zeta potentials of these NPs were characterized to represent their surface charges. The zeta potentials of these NPs show low negative values (in the range of −1.3 to −1.7 mV), which results from the existence of a small amount of carboxyl groups in FITC-labelled PBLG segments. Such a low level of zeta potentials of the NPs could have no profound effect on their cellular internalization behaviors.[30]

Cellular internalization behavior of NPs

The cellular internalization of these NPs was investigated upon incubation with NIH3T3 cells. Fig. 2a shows the overlay confocal laser scanning microscopy (CLSM) images of the cells incubated with various NPs for 8 h. Cell nuclei are stained with 4′,6-diamidino-2-phenylindole (DAPI, blue fluorescence), while the green fluorescence represents FITC-labelled NPs. Compared to the blank group, one can see that the green fluorescence appears in the cells for all the samples after incubation for 8 h, indicating the uptake of the NPs by cells in all the sample groups. The cellular uptake of the NPs is also evidenced by wrinkling and protruding of the cell membranes, as captured from SEM observations. Meanwhile, the distribution of the fluorescently-labelled NPs inside the cells is further detected by CLSM. It is found that the NPs are mainly concentrated in the cytoplasm. The details regarding the SEM and CLSM measurements are provided in the ESI, section 1.7.†

Then, the normalized cellular fluorescence intensity was evaluated by using the cellular fluorescence intensity from CLSM analysis as a function of incubation time (Fig. 2b). The cellular fluorescence intensity is directly proportional to the mass of the internalized NPs. Therefore, the profile of the normalized cellular fluorescence intensity reflects the cellular uptake kinetics for these NPs. To clearly illustrate the influence of the structural characteristics of the NPs on cellular internalization, the fluorescence intensity of the samples incubated for 8 h is analysed (Fig. 2c). It was found that the relative fluorescence intensities for the NPs in group 1 ($R_h \approx 113$ nm) are 0.76, 0.69, and 0.65 for helical rod-1, striped sphere-1, and smooth sphere-1, respectively. As a comparison, the NPs in group 2 ($R_h \approx 165$ nm) show relatively lower fluorescence inten-
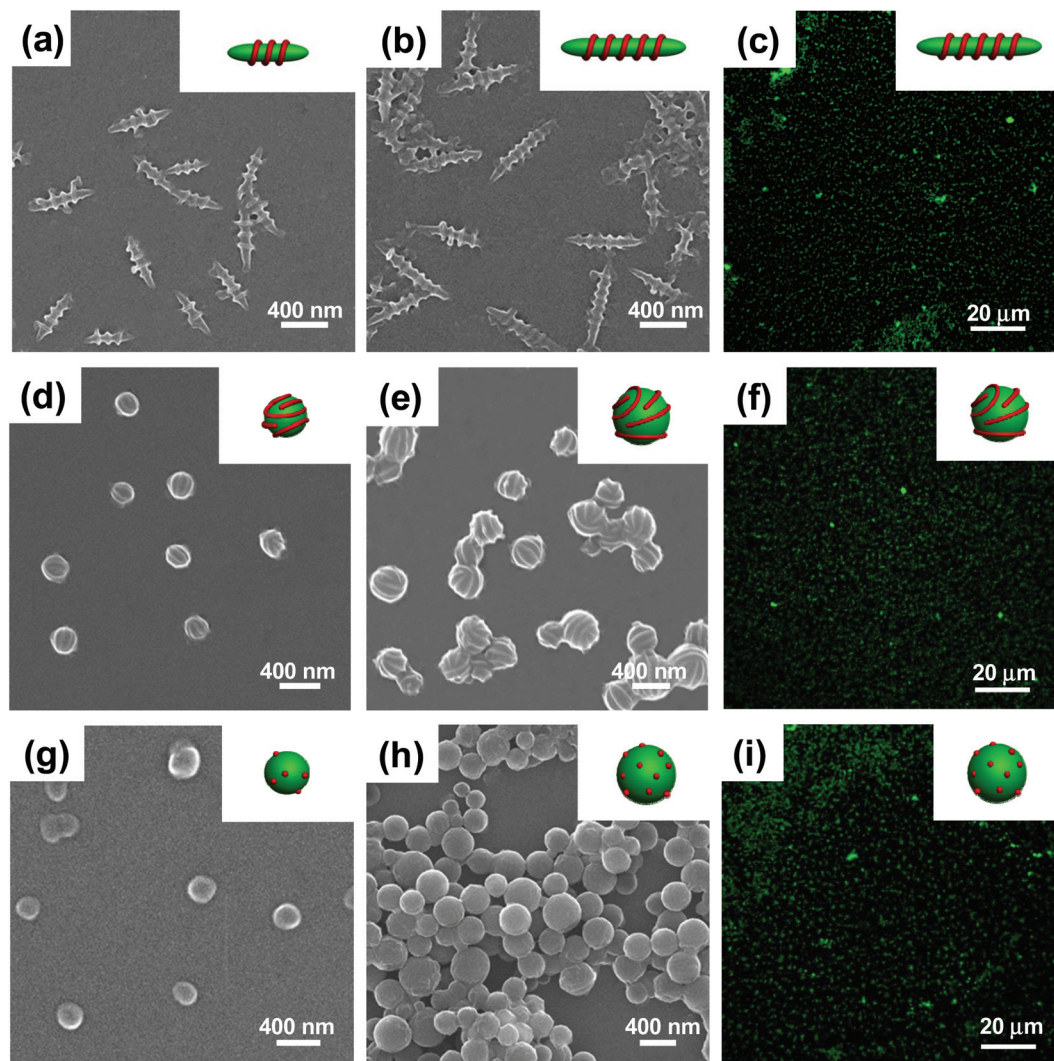
Fig. 1 The morphology and fluorescence characterization of the NPs. SEM images of the NPs: (a) helical rod-1, (b) helical rod-2, (d) striped sphere-1, (e) striped sphere-2, (g) smooth sphere-1, and (h) smooth sphere-2. CLSM images of the NPs in the green channel (FITC): (c) helical rod-2, (f) striped sphere-2, and (i) smooth sphere-2. The insets show schematic illustrations for the corresponding NPs, respectively.

sities (0.61, 0.56, and 0.52 for helical rod-2, striped sphere-2, and smooth sphere-2, respectively). These results indicate that with similar shapes and surface morphologies, the smaller NPs exhibited faster cellular internalization rates. When NPs possess similar R_h values, the helical rods have the fastest uptake rate, followed by the striped spheres and the smooth spheres.

The internalization performance of the NPs was further explored using a flow cytometer (Fig. 3). As can be seen, compared with the blank group (Fig. 3a), all the six types of samples exhibit evident higher intracellular fluorescence intensity (IFI), and the IFI values vary significantly (Fig. 3b–g), indicating that these NPs have entered the cells and their internalization efficiency is very different. Firstly, the smaller NPs exhibited faster cellular internalization rates than their larger counterparts as indicated by the IFI values. The IFI values for smaller NPs are in the range of 122–164, while those

for larger NPs are in the range of 93–111. For the NPs with similar R_h values, both the shape and surface morphology markedly affect the IFI values of the NPs. Taking the NPs in group 1 for example, the helical rods have a larger IFI value (IFI = 164) than the striped spheres (IFI = 137), and the smooth spheres have the smallest IFI value (IFI = 122).

Generally, the uptake of NPs at the size scale of hundreds of nanometers is mediated by energy-dependent endocytosis, which is related to the incubation temperature and hydrolysis of adenosine triphosphate (ATP).[29,54] In order to examine the type of internalization process, we compared the uptake efficiency of these NPs at incubation temperatures of 37 °C and 4 °C, respectively. It was reported that the endocytosis and passive diffusive process could be weakened at low temperature.[54] After 2 h of incubation, the internalization performance of the NPs was quantitatively measured by CLSM. As shown in Fig. 4a, the internalization of the NPs at 4 °C decreased

Table 1 Characteristics of various NPs

	Sample[a]	Schematic model	Radius[b]/nm	Length[b]/nm	R_h[c]/nm	ζ[d]/mV
Group 1	Helical rod-1		52.9 ± 2.6	457.9 ± 16.7	111.2	−1.7 ± 0.3
	Striped sphere-1		109.4 ± 5.8	—	112.9	−1.5 ± 0.1
	Smooth sphere-1		108.5 ± 7.4	—	114.4	−1.3 ± 0.3
Group 2	Helical rod-2		53.3 ± 2.3	679.1 ± 20.4	164.0	−1.5 ± 0.2
	Striped sphere-2		152.0 ± 12.5	—	163.3	−1.3 ± 0.3
	Smooth sphere-2		158.2 ± 11.3	—	168.5	−1.4 ± 0.2

[a] Helical rod-1 and helical rod-2 were prepared using the mixtures of PBLG(FITC)$_{38\,700}$-*b*-PEG$_{5\,000}$/PBLG$_{118\,000}$ and PBLG(FITC)$_{38\,700}$-*b*-PEG$_{5000}$/PBLG$_{300\,000}$ (initial solvent: THF/DMF, 3/7, v/v), respectively. Striped sphere-1 was prepared using PBLG(FITC)$_{38\,700}$-*b*-PEG$_{5000}$/PS$_{10\,000}$ mixtures (initial solvent: THF/DMF, 7/3, v/v). Striped sphere-2 was prepared using PBLG(FITC)$_{38\,700}$-*b*-PEG$_{5000}$/PS$_{19\,400}$ mixtures (initial solvent: THF/DMF, 3/7, v/v). Smooth sphere-1 was prepared using PBLG(FITC)$_{38\,700}$-*b*-PEG$_{5000}$/PBLG$_{28\,000}$ mixtures (initial solvent: THF). Smooth sphere-2 was prepared using PBLG(FITC)$_{38\,700}$-*b*-PEG$_{5000}$/PS$_{19\,400}$ mixtures (initial solvent: DMF). The ratio of block copolymers to homopolymers in these NPs is 4 : 1 in weight, and the preparation temperature is set to 20 °C. [b] The radius and length of the NPs are measured from the SEM images. For the helical rods, the radius refers to the width of the cross section along the short axis. [c] R_h values are obtained by the DLS test (scattering angle is 90°). [d] The zeta potentials of the NPs are measured in Dulbecco's modified Eagle's medium (DMEM) with polymer concentrations of 0.2 g L^{-1}.
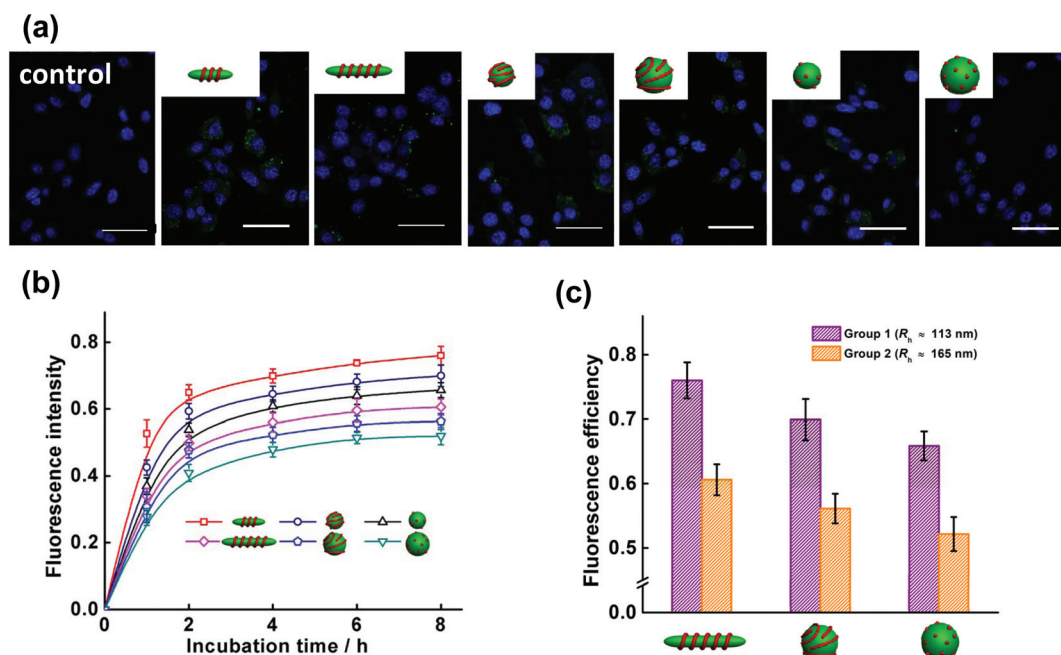

Fig. 2 (a) Overlay CLSM images of NIH3T3 cells upon incubation with various NPs for 8 h. The cell nuclei were stained with DAPI (blue channel), and the FITC labelled block copolymers exhibit green fluorescence. The insets in these images show schematic illustrations for the corresponding NPs, respectively. Scale bar: 50 μm. (b) Normalized fluorescence intensity of NIH3T3 cells quantified from CLSM observation as a function of time. (c) Fluorescence intensity of NIH3T3 cells incubated with various NPs for 8 h.

obviously as compared to that at 37 °C, which indicates that the internalization process of the NPs is mostly controlled by endocytosis. In addition, a biochemical inhibitor, sodium azide/2-deoxyglucose (NaN$_3$/DOG), which is able to inhibit the function of ATP, was also applied to determine whether the internalization process of the NPs is the energy-dependent endocytosis.[26,55] The cellular internalization of the NPs dramatically decreases when the cells were treated with NaN$_3$/DOG (Fig. 4a). It should be noted that the internalization process is not completely inhibited, which is due to the existence of glucose and exogenous ATP in the media. These results demonstrate that the energy-dependent endocytosis is the main pathway for the internalization of the self-assembled NPs.

Furthermore, the cytotoxicity of the NPs also influences their cellular internalization, since they could lead to the frac-
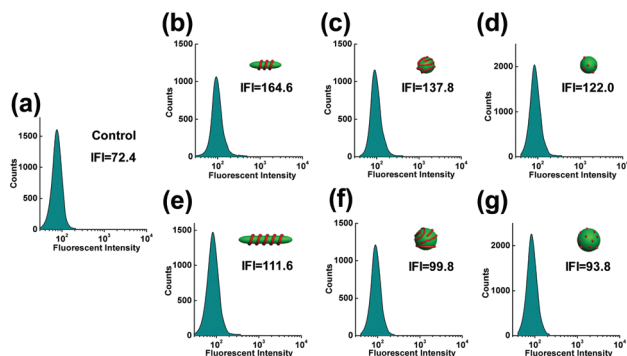
Fig. 3 Cellular fluorescence intensity after incubating with NPs for 6 h measured by flow cytometry: (a) control group, (b) helical rod-1, (c) striped sphere-1, (d) smooth sphere-1, (e) helical rod-2, (f) striped sphere-2, and (g) smooth sphere-2. IFI is a representative of the average intracellular fluorescence intensity.

ture and death of the cells. To ensure the veracity and reliability of the analyses, the cytotoxicities of these NPs are tested by the tetrazolium salt (thiazolyl blue tetrazolium bromide (MTT)) assay (Fig. 4b). After 6 h of incubation, no obvious cytotoxicity of the NPs on the cells was detected. Such results indicate that these self-assembled NPs possess good biocompatibility, and the influence of the cytotoxicity of the NPs can be ruled out in this study.

The above investigations revealed that the studied NPs can be taken up *via* energy-dependent endocytosis, and the NPs with different sizes, shapes and surface morphologies exhibit different uptake efficiencies. Some of the phenomena can be explained according to the literature. For example, it has been reported that the NPs with rough surfaces have higher uptake efficiencies compared to those with smooth surfaces.[26,34] In addition, some studies reveal that the faster cellular internalization for rod-like NPs may result from their higher curvature of the top ends compared to the spherical ones with the same volume, which could reinforce the interaction with the cell membrane.[55,56] However, for the NPs with helical and stripe-pattern surface morphologies, there is a lack of comprehensive and systematic understanding of their high internalization efficiency. The internalization behavior of these NPs may exhibit different processes, which can be deeply explored by theoretical simulations.

CGMD simulation of cellular internalization

Although conclusive results have been obtained from the experiments, some important information remains unclear, such as the specific internalization process of the NPs and the reason for their different cellular internalization efficiencies. As a useful tool, theoretical simulations are ready to address these challenges.[57]

Herein, we used coarse-grained molecular dynamics (CGMD) to investigate the cellular internalization processes of these NPs. The rod-like and spherical model NPs were constructed by coarse-grained beads, in which the hydrophobic
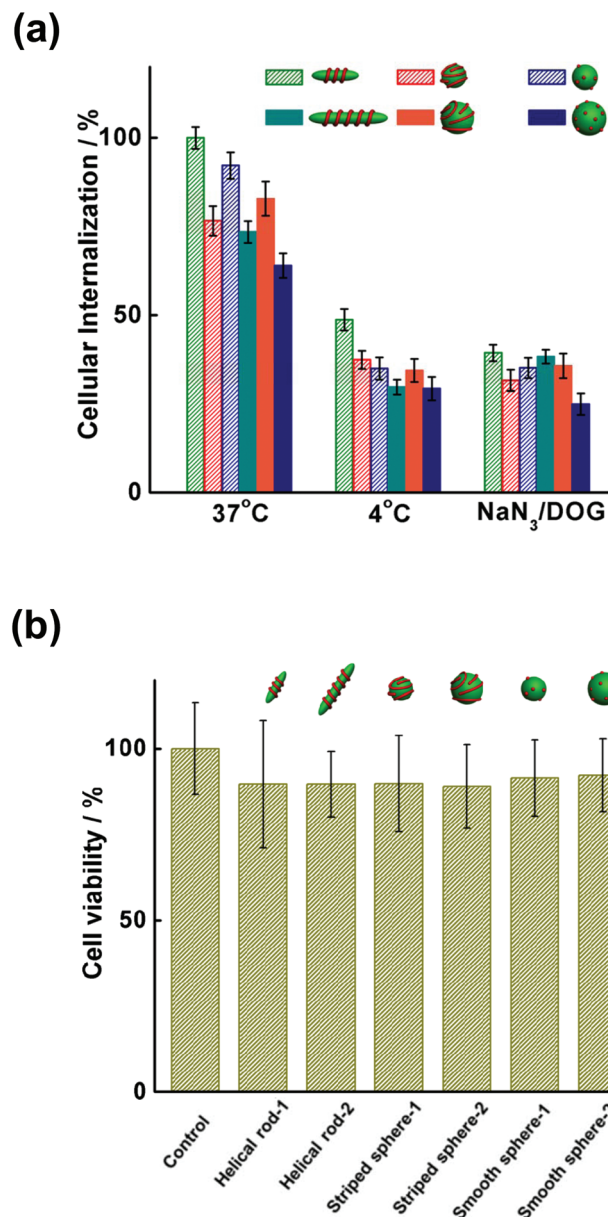
Fig. 4 (a) Cellular internalization of NPs under various conditions (37 °C, 4 °C, and with NaN₃/DOG inhibitor) after incubation for 2 h. Data are represented as average $\pm$ standard deviation (n = 5). (b) Cytotoxicities of the NPs incubated with NIH3T3 cells for 8 h. Each experiment was carried out in septuplicate.

beads act as the substrates and the hydrophilic beads act as the ligand moieties on the substrates. The spherical and rod-like templates correspond to the PS and PBLG cores of the NPs in the experiments,[58] while the ligands on the template denote the methoxy groups at the free ends of the PEG segments. These methoxy groups can bind to the receptor proteins on the plasma membrane *via* relatively weak hydrophobic interactions or hydrogen bonding.[35,59,60] The sizes of the NPs were set in accordance with those in the experiments. For helical rod-1, the diameter (d) is 8σ and the length (l) is 32σ, and for striped sphere-1 and smooth sphere-1, the radius (r) is 8σ,

where σ is the length unit. For the larger NPs (helical rod-2, striped sphere-2, and smooth sphere-2), these size parameters are set as follows: $d = 8\sigma$, $l = 48\sigma$, and $r = 12\sigma$, respectively. In each simulation system, the plasma membrane was formed by 4400 coarse-grained lipids, in which 2200 lipids act as receptors. These receptors can bind to the ligands on the NPs. The ligand on the helical rod is set in a helical manner, and that on the smooth sphere is uniformly distributed. For the striped sphere, the surface ligand is set in a spiral-like manner, which is close to the surface morphology in the experiments. In the simulation box, the NPs were set above the plasma membrane as the initial state of the simulation. As the internalization begins, these NPs get attached to the membrane surfaces.

According to the experimental observations in the present work (Fig. 4a), the cellular uptake of the NPs is an energy-driven process. When the hydrolysis of ATP is inhibited, the internalization of the NPs dramatically decreases. In the simulations, a binding energy between the receptors on the membrane and the ligands on the NPs was set to simulate such an energy-driven internalization process. It was found that in the presence of the ligand–receptor binding, the NPs were taken up by the cells. When the binding energy was set to zero, the NPs cannot be internalized. The details regarding the simulation methods, models, and parameter settings can be found in the Experimental and simulation section in the main text and sections 2.1–2.4 in the ESI.†

The snapshots during the endocytosis of these small NPs are shown in Fig. 5a–c. As can be seen, the NPs are gradually wrapped by lipids and invaginate into the membrane. Finally, the NPs are completely engulfed by the membrane and the lipid-formed vesicles that detach from the membrane. The simulations can provide the endocytosis efficiency of the NPs, which is characterized by the wrapping ratio of the membrane, η (defined as the ratio of the surface area of the NP covered by the membrane to the entire surface area of the NP). The variation of the wrapping ratio for these NPs during the endocytosis process is shown in Fig. 5d. As the endocytosis proceeds, the wrapping ratio is gradually increased, indicating the engulfment of the NPs. The increased rate of the wrapping ratio for the helical rods is the fastest, followed by the striped spheres and the smooth spheres. From the endocytosis process, the complete endocytosis time durations for helical rods, striped spheres, and smooth spheres can be obtained, which are $1.8 \times 10^5\tau$, $2.3 \times 10^5\tau$, and $3.0 \times 10^5\tau$ (τ is the time unit), respectively. These phenomena indicate that the helical rods show the highest endocytosis efficiency, followed by the striped spheres and the smooth spheres. For the NPs with larger sizes, as shown in Fig. 5e, they follow a similar sequence but take a longer time for the endocytosis as compared to the smaller NPs. The details of the simulations regarding the endocytosis of larger NPs can be seen in the ESI, section 2.5.†

Then we performed the simulation of each type of NP 20 times to statistically investigate the uptake efficiency of each type of NP as a function of time. In each simulation, we set one NP above the membrane with the initial distances randomly in the range of 0–20σ. After these 20 simulations, we

examined the internalization percentage as a function of time (Fig. 5f). The simulation results revealed that the uptake percentages of these NPs are all increased with the simulation time. Similar to the case of the wrapping ratio of one NP, the helical rods have the best efficiency and capacity in cellular internalization, followed by the striped spheres and the smooth spheres. In addition, as shown in Fig. 5g, the larger NPs show lower internalization efficiencies, and the structural characteristics (shape and surface morphology) have similar effects on their internalization efficiency as compared to their smaller counterparts. The simulation results are qualitatively in accordance with the experimental observations, although the quantitative match is difficult due to the limitation of the current computational ability.[37]

In order to understand the mechanisms underlying the different uptake performances of these NPs, we further investigated the endocytosis procedure by tracking their movements during the internalization. Herein, the orientations of these NPs as a function of time were calculated (Fig. 6). In the existing theoretical research studies,[61] the endocytosis of the spherical NPs with uniformly decorated ligands has already been explicitly studied. For the smooth spheres, two angles denoted by θ and γ were calculated. Specifically, θ is the angle between the major axis of the NPs and the normal direction of the membrane (z), and γ is the angle that the NP rotates about its major axis. The schematic illustrations of the two angles are provided in the inset in Fig. 6a. The values of the two angles randomly fluctuate around zero, indicating that the rotation of the smooth spheres during the endocytosis is irregular. The fluctuation is so weak that the rotation almost has no effect on the endocytosis procedure.

Interestingly, after examining the rotation angles of the helical rods and the striped spheres, we noted that both the NPs could be endocytosed with precession, which is a unique endocytosis pathway. In order to present this precession behavior, we measured the θ angles and the angle that the major axis of the NPs has rotated around the z direction (denoted by φ) as a function of time (Fig. 6b and c). The schematic illustrations of the two angles in the precessions of the striped sphere and the helical rod are shown in the insets in Fig. 6b and c, respectively. Before $5 \times 10^4\tau$, the φ angles exhibit a sine/cosine-like profile with almost one and two complete periods for the helical rods and striped spheres, respectively. This indicates the two types of NPs precessed for nearly one and two periods, respectively. During this time, the θ angle is relatively small, because a tip-oriented NP would be more favorable for the precession. After that, the φ angle nearly remains unchanged, meaning that the precession behavior stops. The θ angle increases to a large value, resulting in a greater contact angle between NPs and membrane, which benefits the following detachment of the lipid-wrapped NPs from the membrane. According to the variation of the two angles, the endocytosis procedure of the striped spheres and the helical rods can be divided into two stages, namely the precession stage and the precession-free stage. The precession of the striped spheres and helical rods is a unique behavior during the endocytosis,
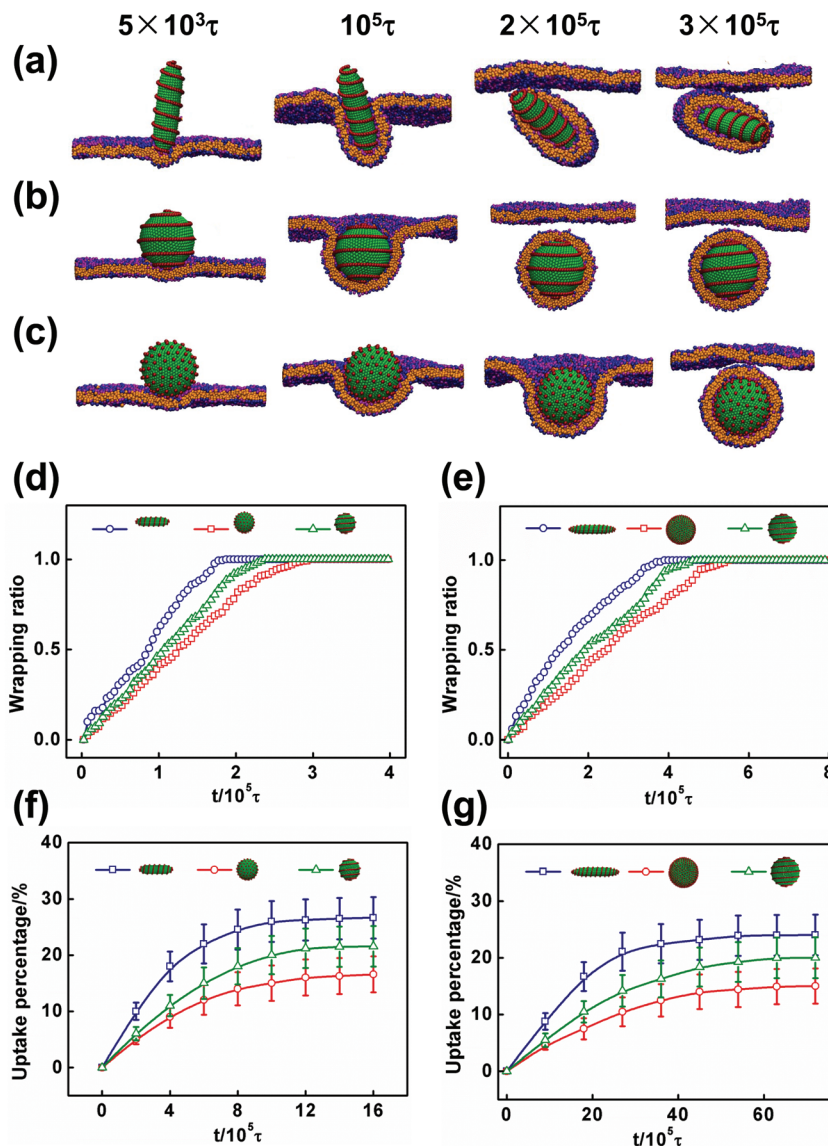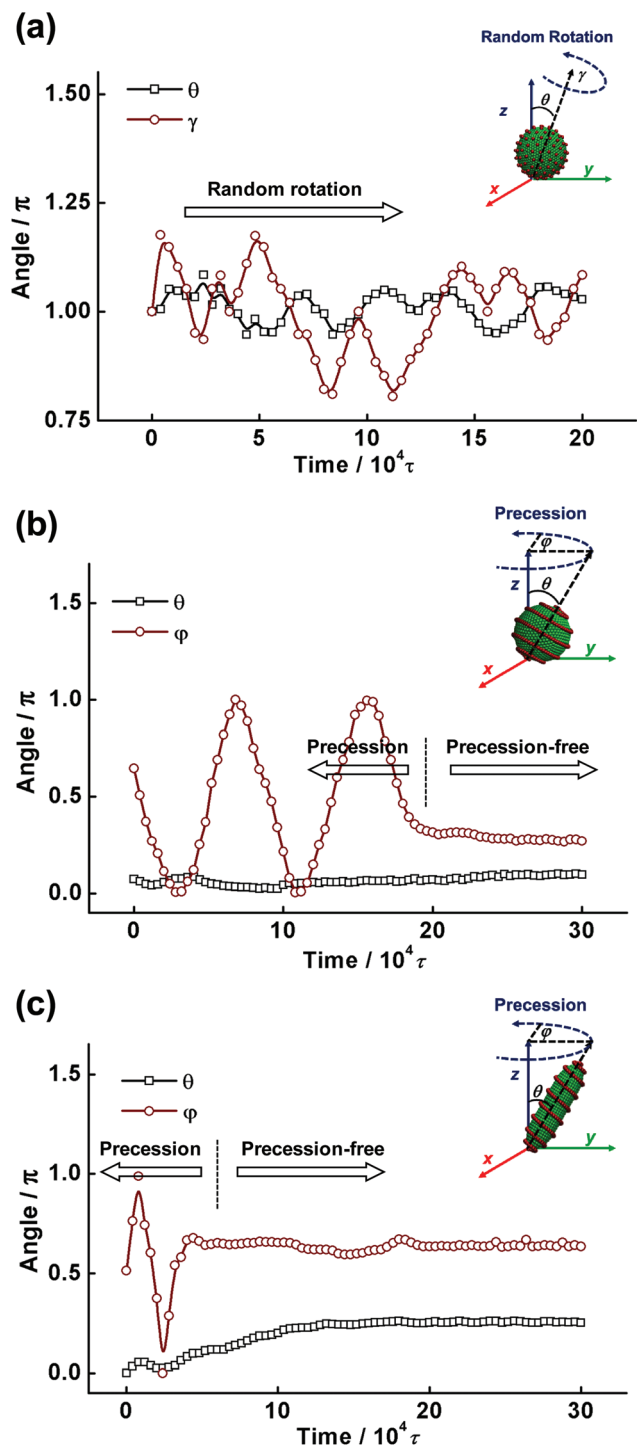
Fig. 5 (a–c) Snapshots during the internalization of small NPs with different shapes and surface morphologies: (a) helical rod, (b) striped sphere, and (c) smooth sphere. (d, e) Profiles of wrapping ratio during the internalization of: (d) small NPs and (e) large NPs; (f, g) profiles of uptake percentage during the internalization of: (f) small NPs and (g) large NPs.

which is contributed by the helical/spiral packing manner of the ligands on the surface of the nanoparticles. When the ligands are uniformly packed mimicking a smooth surface, both the spherical and rod-like nanoparticles can be endocytosed without the precession behavior. This phenomenon can be evidenced by the reports in the literature.[30,37,40] These reports showed that when the precession is excluded, nanoparticles with different shapes would be endocytosed through a similar pathway.

The existing theories can be applied to explain the internalization difference of these studied NPs.[62,63] According to these theoretical studies, the endocytosis efficiency of NPs is directly related to their size (R_h). The larger NP induces a higher energy barrier and a longer wrapping duration, which decrease its internalization efficiency compared to its smaller counter-

part. For the NPs with different shapes (*i.e.*, helical rod and striped sphere), the rod-like NP possesses a smaller surface area than the spherical one with the same R_h value, which results in the shorter wrapping time of the membrane and higher internalization efficiency for the helical rod. Meanwhile, the surface morphology of the NPs could also play an important role in the endocytosis process. The above simulation results reveal that the helical rods or the striped spheres take the precession behavior to get through the membrane, due to their helical or spiral-like surface morphologies, while the smooth spheres enter the cells *via* random rotation. The difference of the internalization pathways for these NPs influences their uptake efficiency. The precession pathway can lower the bending energy of the cell membrane, which is the main energy barrier during the internalization process. The

random rotation process of the smooth sphere makes almost no contribution to the endocytosis efficiency. In this case, the helical rods and the striped spheres have faster internalization rates than the smooth spheres.

The present work provides an insight into the cellular internalization performance of various self-assembled NPs both experimentally and theoretically. It was found that the NPs with different structural characteristics exhibit different internalization efficiencies, which can be attributed to their surface areas and internalization processes. In our system, the NPs with smaller size (R_h), rod-like shape and helical/striped surface show higher internalization efficiencies. It could provide guidance for the design and fabrication of nanocarriers with expected cellular internalization efficiency and be beneficial for the application of polymeric biomaterials in advanced drug delivery systems. In addition, as the helical and the stripe-pattern structures are two general structures in nature, the present findings of the specific internalization pathways of these structures may be helpful in developing potential biomimicking applications. For example, the cellular internalization behavior of NPs with helical/striped surface could provide inspiration to the interaction processes between the viruses with similar surfaces and the host cells.

Conclusions

In summary, the cellular internalization behavior of various self-assembled NPs, including helical rods, striped spheres, and smooth spheres was studied by a combination of experiments and theoretical simulations. The NPs with smaller R_h values exhibit faster internalization rates. For the NPs with similar R_h values, the helical rods show the highest uptake efficiency, followed by the striped spheres and the smooth spheres. Simulations further verified the experimental results and revealed the details for the cellular internalization processes of the NPs. The unique precession internalization process for the helical rod and striped sphere show higher efficiency than the random rotation process for smooth spheres with similar R_h values. In addition, the smaller surface area of the helical rod reduces the wrapping time of the membrane and makes it easier to be taken up compared to the striped sphere. This study not only provides guidance for the design and fabrication of efficient nanocarriers in advanced drug delivery systems, but also facilitates potential biomimicking studies.

Conflicts of interest

There are no conflicts to declare.

Acknowledgements

Fig. 6 (a) θ and γ angles of the smooth sphere as a function of time during the endocytosis procedure. (b) θ and φ angles of the striped sphere as a function of time. The precession and precession-free stages are denoted in the figure. (c) θ and φ angles of the helical rod as a function of time. Insets are schematic illustrations of the random rotation of the smooth sphere NP, the precession of the striped sphere, and the precession of the helical rod, respectively.

References

1 C. Cai, J. Lin, Y. Lu, Q. Zhang and L. Wang, *Chem. Soc. Rev.*, 2016, **45**, 5985–6014.

2 U. Tritschler, S. Pearce, J. Gwyther, G. R. Whittell and I. Manners, *Macromolecules*, 2017, **50**, 3439–3463.

3 M. Huo, Y. Zhang, M. Zeng, L. Liu, Y. Wei and J. Yuan, *Macromolecules*, 2017, **50**, 8192–8201.

4 Z. Zhuang, T. Jiang, J. Lin, L. Gao, C. Yang, L. Wang and C. Cai, *Angew. Chem., Int. Ed.*, 2016, **55**, 12522–12527.

5 Z. Xu, J. Lin, Q. Zhang, L. Wang and X. Tian, *Polym. Chem.*, 2016, **7**, 3783–3811.

6 S. Mura, J. Nicolas and P. Couvreur, *Nat. Mat.*, 2013, **12**, 991–1003.

7 W. Chen, Y. Zou, F. Meng, R. Cheng, C. Deng, J. Feijen and Z. Zhong, *Biomacromolecules*, 2014, **15**, 900–907.

8 N. Ngandeu, M. Gella, Y. Opoku-Damoah, X. Gu, Y. Han, J. Zhou and Y. Ding, *Biomater. Sci.*, 2018, **6**, 958–973.

9 D. Kakkar, S. Mazzaferro, J. Thevenot, C. Schatz, A. Bhatt, B. S. Dwarakanath, H. Singh, A. K. Mishra and S. Lecommandoux, *Macromol. Biosci.*, 2015, **15**, 124–137.

10 L. Chen, T. Jiang, C. Cai, L. Wang, J. Lin and X. Cao, *Adv. Healthcare Mater.*, 2014, **3**, 1508–1517.

11 S. B. Hartono, W. Gu, F. Kleitz, J. Liu, L. He, A. P. J. Middelberg, C. Yu, G. Lu and S. Qiao, *ACS Nano*, 2012, **6**, 2104–2117.

12 J. Look, N. Wilhelm, H. von Briesen, N. Noske, C. Günther, K. Langer and E. Gorjup, *Mol. Pharm.*, 2015, **12**, 3202–3213.

13 J. Mikkila, A. P. Eskelinen, E. H. Niemela, V. Linko, M. J. Frilander, P. Torma and M. A. Kostiainen, *Nano Lett.*, 2014, **14**, 2196–2200.

14 Y. Li, T. Thambi and D. S. Lee, *Adv. Healthcare Mater.*, 2018, **7**, 1700886.

15 H. Zhu, P. Cheng, P. Chen and K. Pu, *Biomater. Sci.*, 2018, **6**, 746–765.

16 L. Cheng, K. Yang, Y. Li, X. Zeng, M. Shao, S.-T. Lee and Z. Liu, *Biomaterials*, 2012, **33**, 2215–2222.

17 N. Lee, H. R. Cho, M. H. Oh, S. H. Lee, K. Kim, B. H. Kim, K. Shin, T.-Y. Ahn, J. W. Choi, Y.-W. Kim, S. H. Choi and T. Hyeon, *J. Am. Chem. Soc.*, 2012, **134**, 10309–10312.

18 L. Liu, R. Wang, C. Wang, J. Wang, L. Chen and J. Cheng, *Biomater. Sci.*, 2018, **6**, 997–1001.

19 A. G. Denkova, R. M. de Kruijff and P. Serra-Crespo, *Adv. Healthcare Mater.*, 2018, **7**, 1701211.

20 A. A. Saei, M. Yazdani, S. E. Lohse, Z. Bakhtiary, V. Serpooshan, M. Ghavami, M. Asadian, S. Mashaghi, E. C. Dreaden, A. Mashaghi and M. Mahmoudi, *Chem. Mater.*, 2017, **29**, 6578–6595.

21 L. Adamiak, M. A. Touve, C. L. M. LeGuyader and N. C. Gianneschi, *ACS Nano*, 2017, **11**, 9877–9888.

22 S. D. Conner and S. L. Schmid, *Nature*, 2003, **422**, 37–44.

23 Q. Sun, T. Ishii, K. Kanehira, T. Sato and A. Taniguchi, *Biomater. Sci.*, 2017, **5**, 1014–1021.

24 S. A. Kulkarni and S. S. Feng, *Pharm. Res.*, 2013, **30**, 2512–2522.

25 A. M. Bannunah, D. Vllasaliu, J. Lord and S. Stolnik, *Mol. Pharm.*, 2014, **11**, 4363–4373.

26 X. Hu, J. Hu, J. Tian, Z. Ge, G. Zhang, K. Luo and S. Liu, *J. Am. Chem. Soc.*, 2013, **135**, 17617–17629.

27 H. Meng, S. Yang, Z. Li, T. Xia, J. Chen, Z. Ji, H. Zhang, X. Wang, S. Lin, C. Huang, H. Zhou, J. I. Zink and A. E. Nel, *ACS Nano*, 2011, **5**, 4434–4447.

28 S. Venkataraman, J. L. Hedrick, Z. Y. Ong, C. Yang, P. L. R. Ee, P. T. Hammond and Y. Y. Yang, *Adv. Drug Delivery Rev.*, 2011, **63**, 1228–1246.

29 O. Shimoni, Y. Yan, Y. Wang and F. Caruso, *ACS Nano*, 2013, **7**, 522–530.

30 S. Zhang, H. Gao and G. Bao, *ACS Nano*, 2015, **9**, 8655–8671.

31 J. Xue, Z. Guan, J. Lin, C. Cai, W. Zhang and X. Jiang, *Small*, 2017, **13**, 1604214.

32 M. Massignani, C. LoPresti, A. Blanazs, J. Madsen, S. P. Armes, A. L. Lewis and G. Battaglia, *Small*, 2009, **5**, 2424–2432.

33 X. Xu, H. Yuan, J. Chang, B. He and Z. Gu, *Angew. Chem., Int. Ed.*, 2012, **51**, 3130–3133.

34 Y. Niu, M. Yu, S. B. Hartono, J. Yang, H. Xu, H. Zhang, J. Zhang, J. Zou, A. Dexter, W. Gu and C. Yu, *Adv. Mater.*, 2013, **25**, 6237.

35 Y. Li, M. Kröger and W. K. Liu, *Biomaterials*, 2014, **35**, 8467–8478.

36 J. Sun, L. Zhang, J. Wang, Q. Feng, D. Liu, Q. Yin, D. Xu, Y. Wei, B. Ding, X. Shi and X. Jiang, *Adv. Mater.*, 2015, **27**, 1402–1407.

37 X. Shi, A. von dem Bussche, R. H. Hurt, A. B. Kane and H. Gao, *Nat. Nanotechnol.*, 2011, **6**, 714–719.

38 H. Ding and Y. Ma, *Small*, 2015, **11**, 1055–1071.

39 J. Liang, P. Chen, B. Dong, Z. Huang, K. Zhao and L.-T. Yan, *Biomacromolecules*, 2016, **17**, 1834–1844.

40 Y. Li, T. Yue, K. Yang and X. Zhang, *Biomaterials*, 2012, **33**, 4965–4973.

41 I. R. Cooke and M. Deserno, *J. Chem. Phys.*, 2005, **123**, 224710.

42 H. J. C. Berendsen, J. P. M. Postma, W. F. van Gunsteren, A. DiNola and J. R. Haak, *J. Chem. Phys.*, 1984, **81**, 3684–3690.

43 G. S. Grest and K. Kremer, *Phys. Rev. A*, 1986, **33**, 3628–3631.

44 G. S. Grest, M. D. Lacasse, K. Kremer and A. M. Gupta, *J. Chem. Phys.*, 1996, **105**, 10583–10594.

45 G. K. Bourov and A. Bhattacharya, *J. Chem. Phys.*, 2003, **119**, 9219–9225.

46 C. Cai, J. Lin, X. Zhu, S. Gong, X.-S. Wang and L. Wang, *Macromolecules*, 2016, **49**, 15–22.

47 C. Cai, Y. Li, J. Lin, L. Wang, S. Lin, X.-S. Wang and T. Jiang, *Angew. Chem., Int. Ed.*, 2013, **52**, 7732–7736.

48 S. Zhang, C. Cai, Z. Guan, J. Lin and X. Zhu, *Chin. Chem. Lett.*, 2017, **28**, 839–844.

49 X. Zhu, Z. Guan, J. Lin and C. Cai, *Sci. Rep.*, 2016, **6**, 29796.

50 Z. Guan, L. Wang, X. Zhu and J. Lin, *Mater. Chem. Front.*, 2016, **1**, 697–708.

51 C. Dong and J. Irudayaraj, *J. Phys. Chem. B*, 2012, **116**, 12125–12132.

52 J. P. Best, Y. Yan and F. Caruso, *Adv. Healthcare Mater.*, 2012, **1**, 35–47.

53 C. Y. Tay, M. I. Setyawati, J. Xie, W. J. Parak and D. T. Leong, *Adv. Funct. Mater.*, 2014, **24**, 5936–5955.

54 C. Liu, X. Zhen, X. Wang, W. Wu and X. Jiang, *Soft Matter*, 2011, **7**, 11526–11534.

55 S. E. Gratton, P. A. Ropp, P. D. Pohlhaus, J. C. Luft, V. J. Madden, M. E. Napier and J. M. DeSimone, *Proc. Natl. Acad. Sci. U. S. A.*, 2008, **105**, 11613–11618.

56 X. Huang, X. Teng, D. Chen, F. Tang and J. He, *Biomaterials*, 2010, **31**, 438–448.

57 Q. Zhang, J. Lin, L. Wang and Z. Xu, *Prog. Polym. Sci.*, 2017, **75**, 1–30.

58 Z. Guan, L. Wang and J. Lin, *Biomacromolecules*, 2017, **18**, 797–807.

59 L. D. Unsworth, H. Sheardown and J. L. Brash, *Langmuir*, 2008, **24**, 1924–1929.

60 C. D. Walkey, J. B. Olsen, H. Guo, A. Emili and W. C. W. Chan, *J. Am. Chem. Soc.*, 2012, **134**, 2139–2147.

61 R. Vácha, F. J. Martinez-Veracoechea and D. Frenkel, *Nano Lett.*, 2011, **11**, 5391–5395.

62 W. Helfrich, *Z. Naturforsch., C: Biochem., Biophys., Biol., Virol.*, 1973, **28**, 693–703.

63 H. Gao, W. Shi and L. B. Freund, *Proc. Natl. Acad. Sci. U. S. A.*, 2005, **102**, 9469–9474.